Electronic Supplementary Information

Self-supported Ni/NiO heterostructures with controlled reduction protocol for enhanced industrial alkaline hydrogen evolution

Haiyang Wang[a], Cong Chen*[a], Junxia Shen[a], Pierre-Yves Olu[b], Longhui Li[c], Wen Dong[a], Ronglei Fan*[a] and Mingrong Shen*[a]

[a]*School of Physical Science and Technology, Jiangsu Key Laboratory of Frontier Material Physics and Devices, Collaborative Innovation Center of Suzhou Nano Science and Technology, Soochow University, 1 Shizi Street, Suzhou 215006, Chin*a

[b]*John Cockerill Hydrogen S.A, 1 Rue Jean Potier, 4100 Seraing, Belgium*

[c]*Zhejiang Jiafeili New Material Co, Ltd, No. P (2022)06 Longpan Mountain Block, Yunfeng Street Industrial Park, Lishui 323301, China*

*E-mail: cchen96@suda.edu.cn, rlfan@suda.edu.cn, mrshen@suda.edu.cn

Experimental section

Materials

Sodium borohydride ($NaBH_4$), ethanol (C_2H_5OH), potassium hydroxide (KOH) and hydrochloric acid (HCl) were of analytical grade and used without further. Deionized water with a resistivity of about 18.5 MΩ was used throughout the experimental processes. Nickel mesh (NM) and Raney Ni were purchased from BaoShiLai New Material Technology (Suzhou) Co., Ltd.

Preparation of L-NM

Firstly, the NM (100 cm^2) was soaked in 20% HCl, ethanol and deionized water for 10 min to remove surface oxide layer and other impurities, respectively. Then, as-treated NM was placed on the operation platform of laser system, where NM was ablated by a pulse fiber laser device of LYFB-50 in air atmosphere. The laser operated at a pulse width of 10 ns, 50 W in maximum power, laser speed of 100 mm/s, frequence of 25 KHz. The whole number of processing is five. This sample was called as L-NM.

Preparation of RL-NM

As-prepared L-NM was cut into 1 cm^2 and immersed into 0.5 M $NaBH_4$ solution for 5-30 min. After treatment, this sample was rinsed with deionized water and dried by high purity nitrogen. This sample was called as RL-NM.

Preparation of NiO/L-NM

As-prepared L-NM was placed into tube furnace. The L-NM was annealed at 600℃ with a ramping rate of 3℃/min under air atmosphere for 3h. The obtained sample was called as NiO/L-NM.

Material characterization

The surface morphology was observed by a scanning electron microscope (SEM) (Su-8010, Hitachi), and the change in crystal microstructure was detected by X-ray diffraction (XRD) (D/MAX-2000PC, Rigaku). The surface chemical structure was detected by Raman (HR800, Jobin Yvon, λ=532 nm) and the detection depth is about 100 nm. The surface element valence states were characterized by X-ray photoelectron spectroscopy (XPS) (ESCALAB 250Xi, Thermo) and the detection depth is about 2 nm.

Electrochemical measurements

In laboratory conditions, HER activity were performed using an electrochemical workstation (Biologic, SP200) in a standard three-electrode system, which was consisted of a working electrode, counter electrode (carbon rod) and reference electrode (saturated Ag/AgCl (3 M)). All the measurements were tested in 1 M KOH solution (pH=13.6) at 25 ℃. The potentials were converted to the potentials referring to the reversible hydrogen electrode (RHE), according to following equation: $V_{RHE} = V_{Ag/AgCl} + 0.197\,V + pH \times 0.059\,V$. Electrochemical impedance spectroscopy (EIS) was tested at the frequence from 0.1 Hz to 100 KHz. iR compensation corrections were also applied on the linear sweep voltammetry (LSV) curves based on the obtained value of R through of electrochemical impedance spectroscopy (EIS). In industrial conditions, the assembled two-electrode cells were tested in 30 wt% KOH, 80℃. Tafel slopes are used to assess the HER reaction kinetics, which can be expressed as following equation: $V_{op} = blog\,(J) + a$. (J: current density, b: Tafel slope, V_{op}: Overpotential).

Cycle voltammetry (CV) measurements were used to assess corresponding electrode surface area, which conducted to collect electrochemical double layer capacitance (C_{dl}). CVs were carried out at following conditions: 20-140 mV/s. Capacitive currents (i_{dl}) is the difference value at 0.14V_{RHE}. The electrochemically active surface areas (ECSAs) were obtained, according to following equation: ECSAs = $\frac{C_{dl}}{C_S} \times$ A, (C_s: 0.04 mF cm^{-2}, and A: 1 cm^2).

Turnover frequence (TOF) for various catalysts were conducted by the equation: RF = $\frac{C_{dl}}{C_S}$, where the C_{dl} is obtained by the CV test. C_s is 0.04 mF cm^{-2}, RF is relative roughness factor. The number of surface active sites per cm^{-2} (N) is evaluated by the equation: N = RF × n_s. n_s: 1.761×10^{15} (the number of surface active sites). The TOF for HER is conducted by following equation: TOF= $\frac{j \times N_A}{2NF}$, where j: current density (A cm^{-2}), NA: 6.022×10^{23} (Avogadro constant), F: 96485 C mol^{-1} (Faraday constant)

The wetting ability of sample surface was characterized by surveying the contact angles of electrolyte (1 M KOH solution). A 4 μL droplet of 1 M KOH was dropped on the surface of the electrode and the contact angle was measured by JC2000DM system at room temperature. Each contact angle measurement was repeated more than 3 times. The images of hydrogen bubble release were obtained by a high-speed digital camera system.

Calculation of electricity-to-hydrogen energy conversion efficiency

The electricity-to-hydrogen energy conversion efficiency (η) and unit electricity consumption per cubic meter hydrogen (E_{H_2}, $KW\ h\ Nm^{-3}$) were calculated with the unit electric quantity per cubic meter hydrogen (Q_u, $A\ h\ Nm^{-3}$) and cell voltage (V, V) at industrially required current density of 400 mA cm^{-2} as following, where 1.48 V represents the thermal-neutral voltage of overall water splitting, e and N_A are the electron charge and Avogadro number, respectively.

$Q_u = 2N_A e/(3600 \times 22.43 \times 10^{-3}) = 2390\ A\ h\ Nm^{-3}$

For the RL-NM||Ni electrolyzer,

$E_{H_2} = Q_u \times V/1000 = 2390 \times 1.791 \div 1000 = 4.280\ KW\ h\ Nm^{-3}$

$$\eta = \frac{1.48 \times Q_u}{E_{H_2} \times 1000} \times 100\% = \frac{1.48 \times 2390}{4.280 \times 1000} \times 100\% = 82.6\%$$

For the Raney Ni||Ni electrolyzer,

$E_{H_2} = Q_u \times V/1000 = 2390 \times 1.887 \div 1000 = 4.509\ KW\ h\ Nm^{-3}$

$$\eta = \frac{1.48 \times Q_u}{E_{H_2} \times 1000} \times 100\% = \frac{1.48 \times 2390}{4.509 \times 1000} \times 100\% = 78.4\%$$

Theoretical calculation

We used the Vienna ab initio simulation package (VASP) to perform the first principles calculations[1, 2]. The interaction between the atomic cores and electrons were described according to the projector augmented wave (PAW), with the plane wave cutoff of 400 eV and spin polarization[3]. The semi-local exchange and correlation energies were described by the Generalized Gradient Approximation (GGA) with the Perdew-Burke-

Ernzerhof (PBE) exchange-correlation functional[4]. The (3×3) Ni (111) and (2×2) NiO (111) surface were both modeled by five-atomic layer slabs, and a vacuum layer of 15 Å was applied between adjacent slabs to eliminate the interaction by periodic condition along the normal direction of surface. The NiO/Ni model consists of Ni (111) structure and Ni (111) structure covered by one O atoms to mimic the controlled ratio of NiO/Ni by reduction process. The atoms in the top three layers were fully relaxed, while the rest of the atoms were fixed in the equilibrium positions. A Monkhosrt-Pack grid 3×3×1 was used to carry out the calculations. The convergence criterion was set to 10^{-4} eV for total energies and 0.02 eV/Å for total forces. The Gibbs free energy change ΔG were evaluated by the formula[5, 6].

$\Delta G=\Delta E+\Delta ZPE-T\Delta S$

where E is the total energy, ZPE is the zero-point energy, T is the temperature, and S is the entropy. The nudged elastic band (NEB) method was used to find the transition state in the water dissociation step in the HER[7].

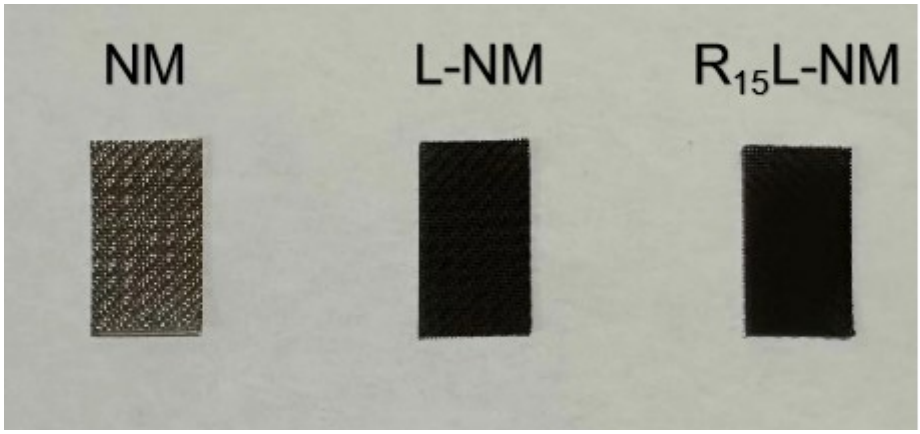

Figure S1. Photograph of NM, L-NM and R_{15}L-NM (the size is 1cm×2cm)

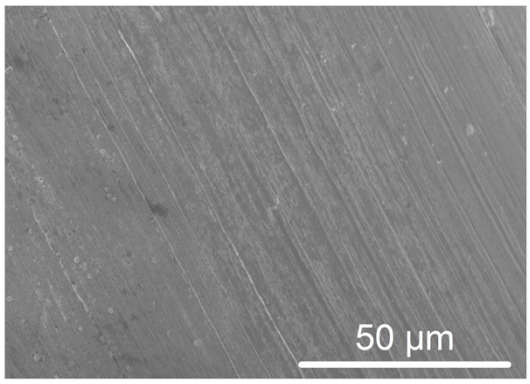

Figure S2. SEM image of NM.

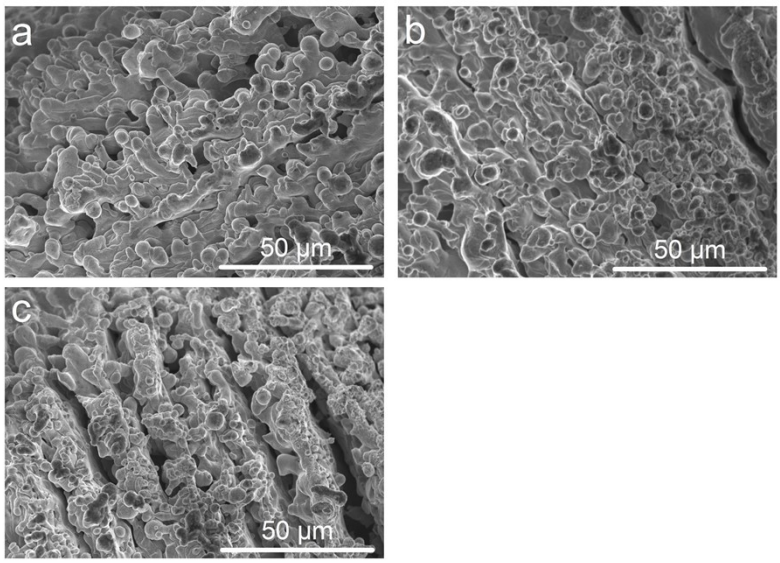

Figure S3. SEM images of (a) R_5L-NM, (b) R_{10}L-NM and (c) R_{30}L-NM.

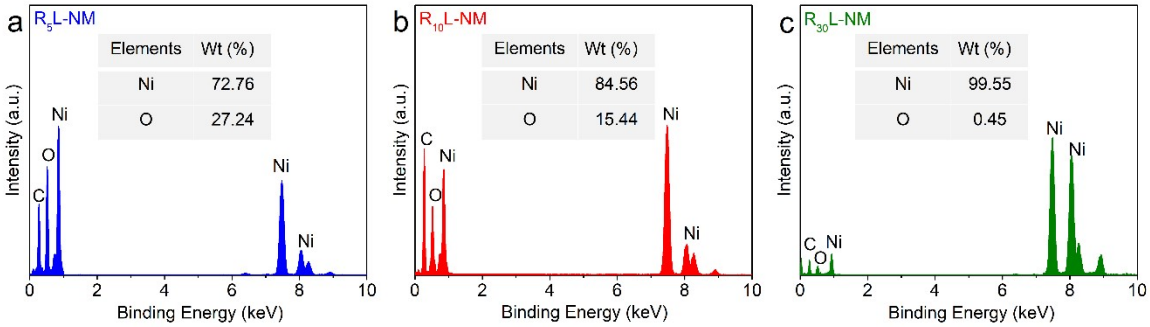

Figure S4. EDX spectra of (a) R_5L-NM, (b) R_{10}L-NM and (c) R_{30}L-NM.

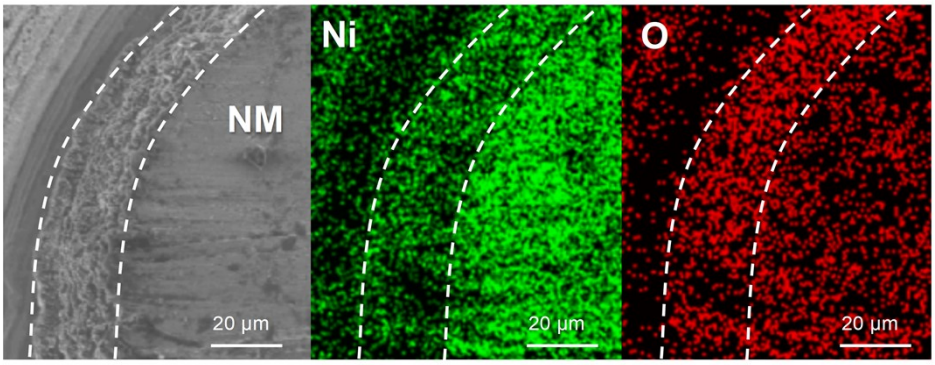

Figure S5. Cross-sectional SEM image and EDX mapping images of RL-NM (Dotted region represents NiO/Ni heterostructure catalysts).

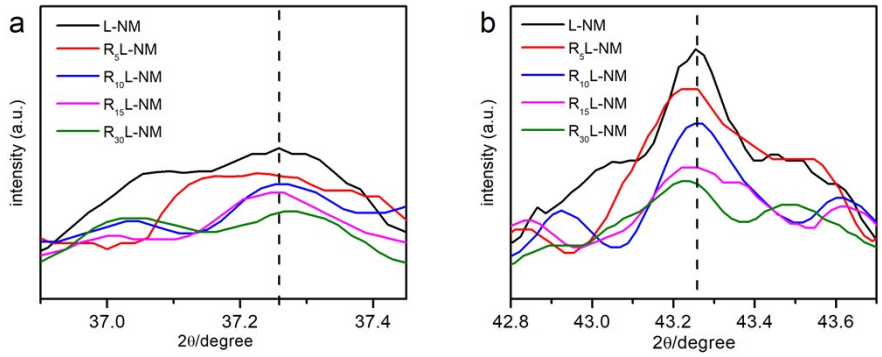

Figure S6. XRD patterns of L-NM, R_5L-NM, R_{10}L-NM, R_{15}L-NM and R_{30}L-NM.

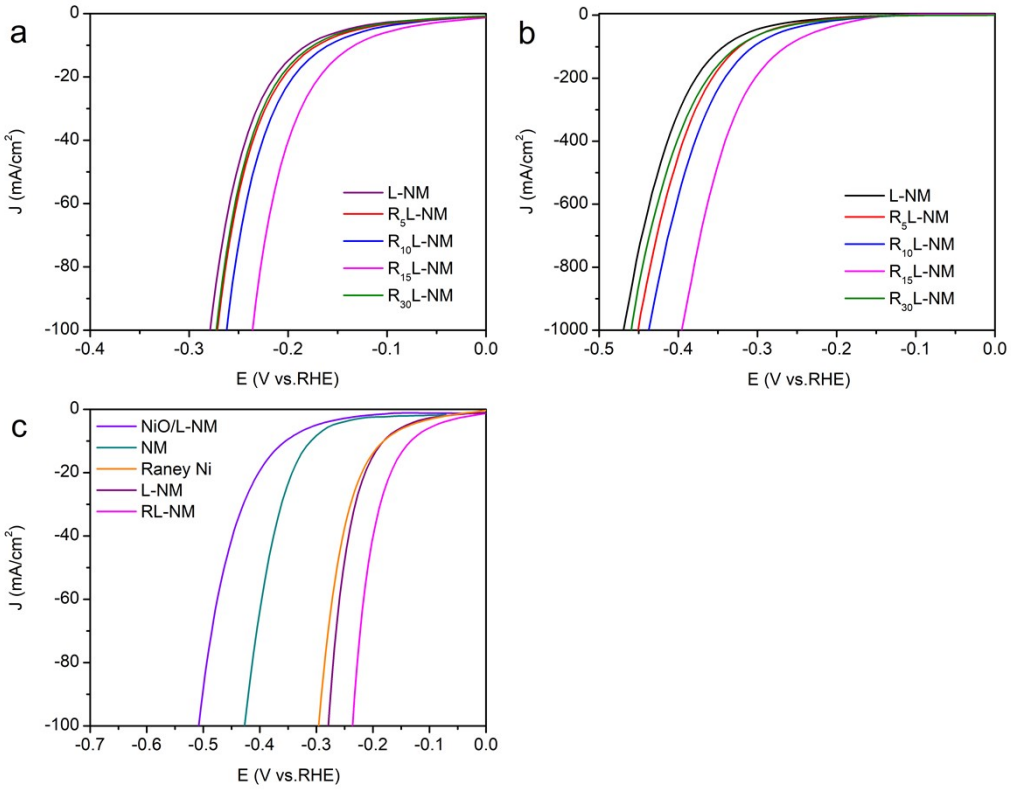

Figure S7. The optimal HER LSV curves for L-NM with different reduction time in (a) laboratory conditions and (b) industrial conditions. (c) LSV curves for NiO/L-NM, NM, Raney Ni, L-NM and RL-NM in laboratory conditions

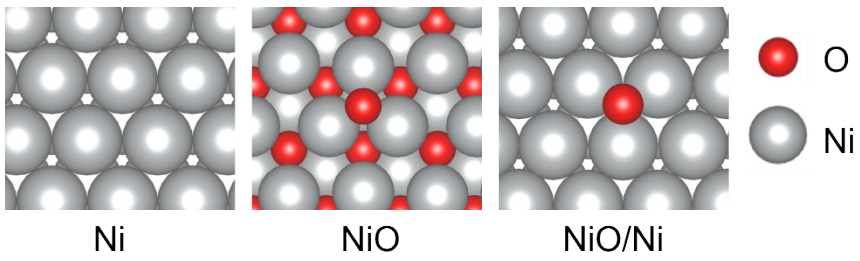

Figure S8. The slab model of Ni, NiO and NiO/Ni.

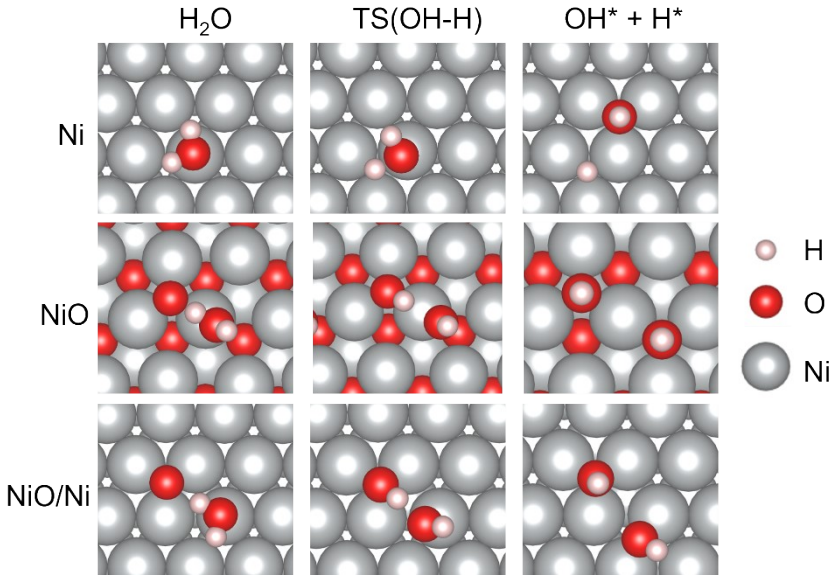

Figure S9. The initial states, transition states (TS) and final states of the water dissociation process for Ni, NiO and NiO/Ni.

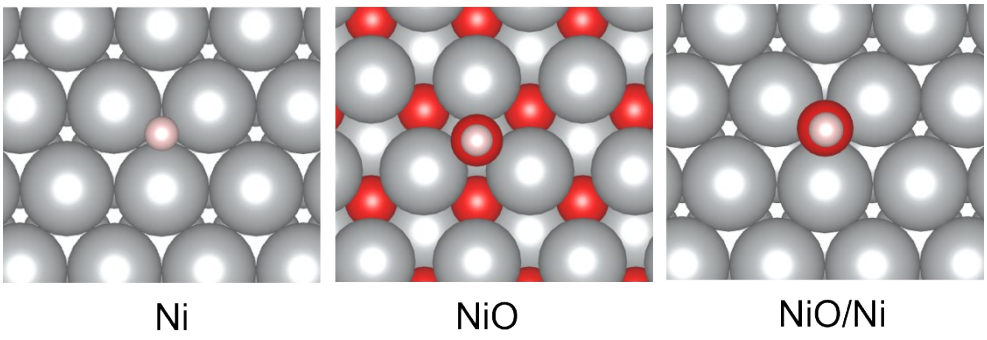

Figure S10. Active sites on Ni, NiO and NiO/Ni.

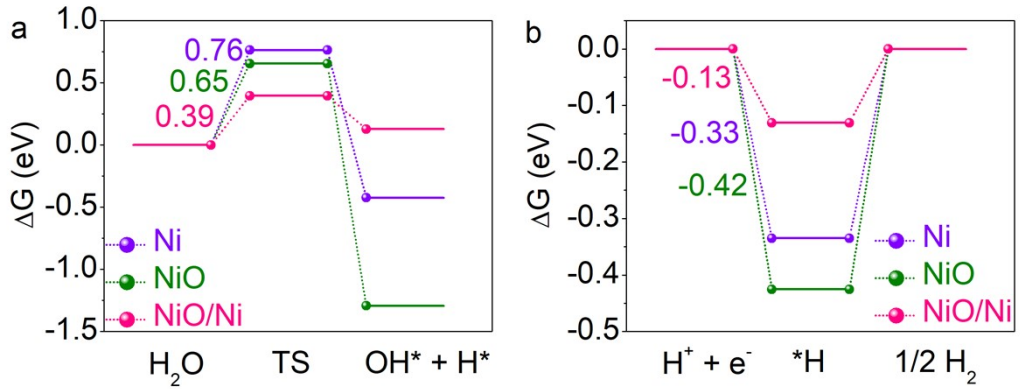

Figure S11. (a) Calculated energy barrier of water dissociation and (b) H* adsorption-free energy on Ni, NiO and NiO/Ni.

To reveal the significance of reduction process, we have performed the theoretical calculations to reveal the active sites and their roles for the HER. As shown in Fig. S8, S9 and S10, the slab models of Ni, NiO and NiO/Ni are established. The product states and adsorption sites were referred to previous studies[8-10]. Especially, the NiO/Ni model consists of Ni (111) structure and Ni (111) structure covered by one O atoms to mimic the controlled ratio of NiO/Ni by reduction process. Notably, the energy barrier of water dissociation (ΔG (H_2O)) on the NiO/Ni is calculated to be 0.39 eV, which is smaller than that of Ni (0.76 eV) and NiO (0.65 eV), indicating that the controlled ratio of Ni and NiO can improve water dissociation ability (Fig. S11a). Fig. RS11b is the H* adsorption-free energy ($\Delta G(H^*)$) for different samples, which is an important quantity to assess catalytic activity. $|\Delta G(H^*)|$ value of NiO/Ni is as low as 0.13 eV, almost half of that for Ni (0.33 eV) and NiO (0.42 eV). Indeed, the $\Delta G(H^*)$ tends to approach zero, making H* adsorption and desorption as well as H_2 production easier. Based on the above results, we can conclude that the controlled ratio of NiO/Ni heterostructure can accelerate the water dissociation and hydrogen adsorption/desorption, in comparison to single Ni or NiO, thus displaying the best HER activity.

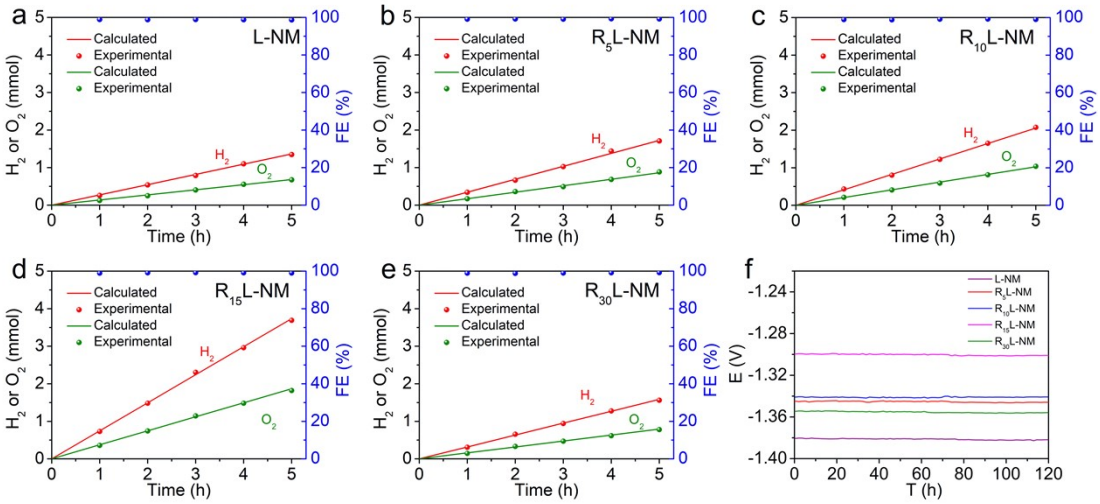

Figure S12. The Faradaic efficiency of (a) L-NM, (b) R_5L-NM, (c) R_{10}L-NM, (d) R_{15}L-NM and (e) R_{30}L-NM (The test voltage is -0.2V). (f) The stability of various samples under 1 M KOH, 25℃.

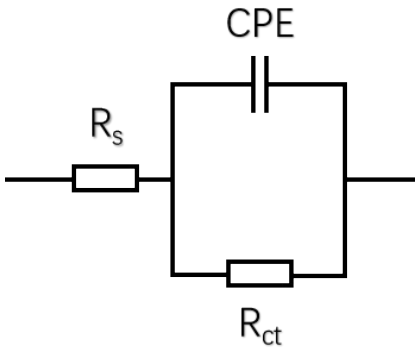

Figure S13. The equivalent circuit model corresponding to the charge transfer from the NM to the electrolyte for NiO/L-NM, NM, Raney Ni, L-NM and RL-NM catalysts.

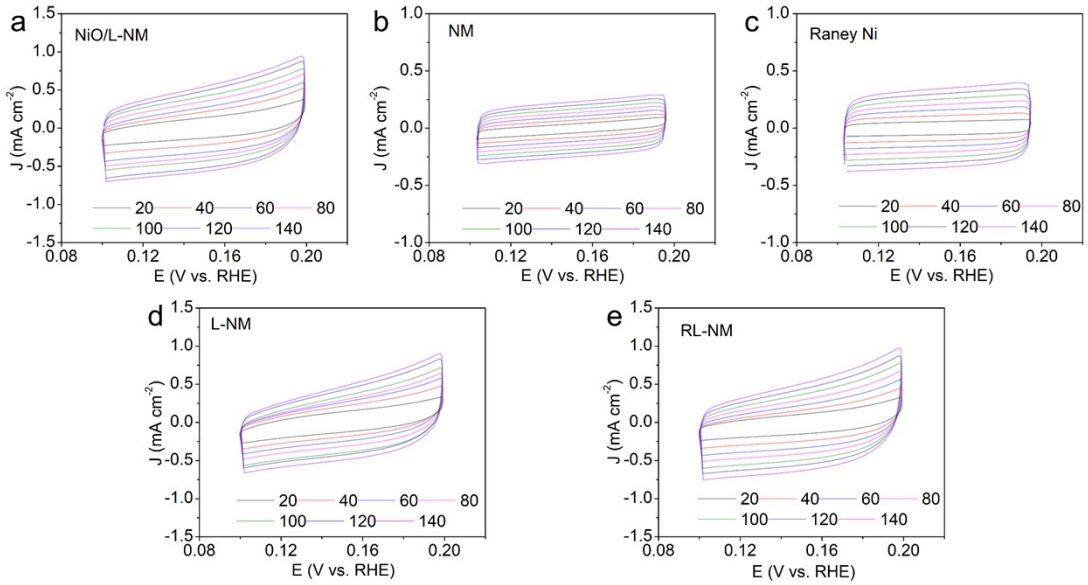

Figure S14. Cyclic voltammetry for HER at the scan rates of 20, 40, 60, 80, 100, 120 and 140 mV/s in the range of no faradaic processes for (a) NiO/L-NM, (b) NM, (c) Raney Ni, (d) L-NM and (e) RL-NM.

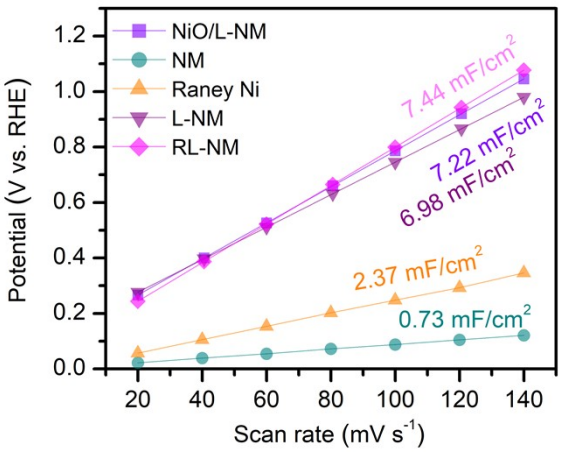

Figure S15. Double-layer capacitances for NiO/L-NM, NM, Raney Ni, L-NM and RL-NM.

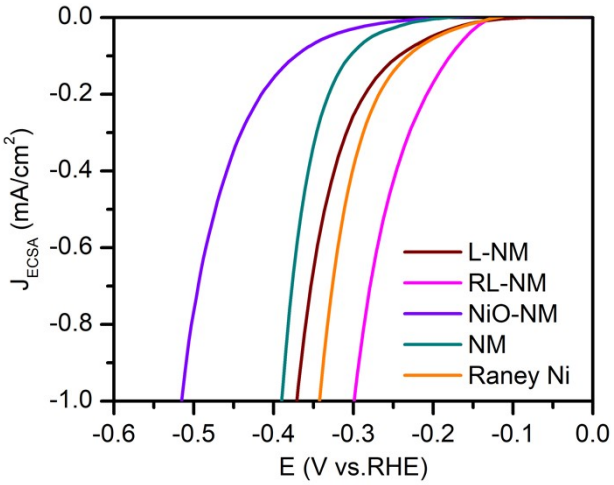

Figure S16. LSV curves normalized by ECSA of the NiO/L-NM, L-NM, Raney Ni and RL-NM electrodes.

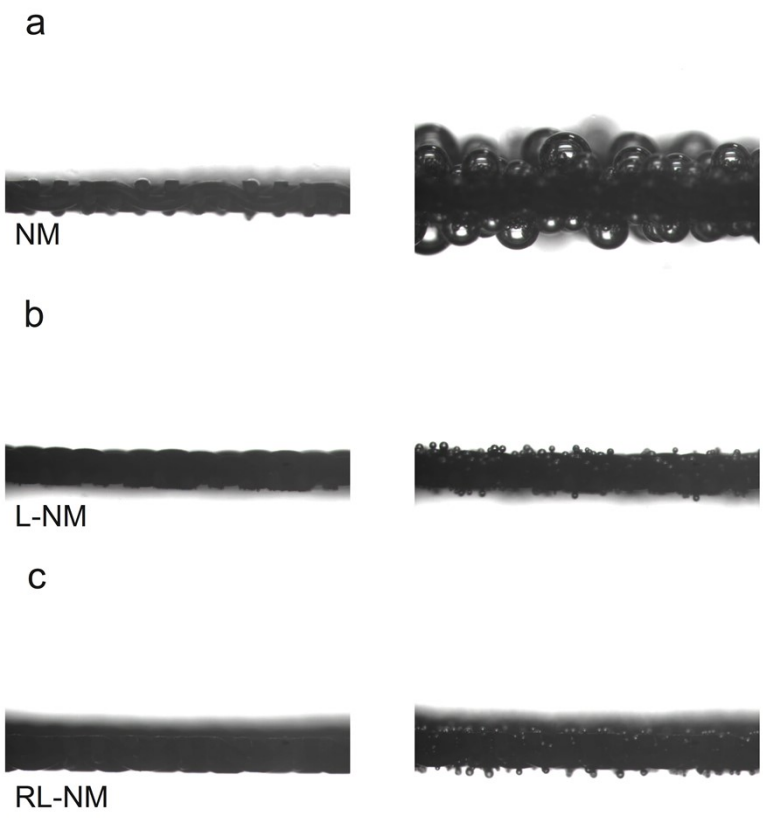

Figure S17. Digital images of the H_2 bubbles released from (a) NM, (b) L-NM and (c) RL-NM at -100 mA cm^{-2}.

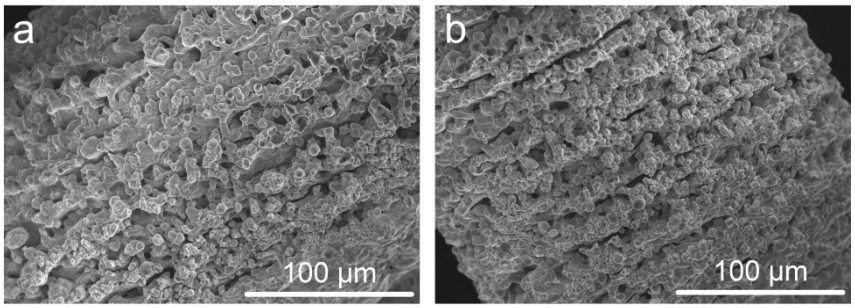

Figure S18. SEM images of RL-NM. (a) before and (b) after lifetime test.

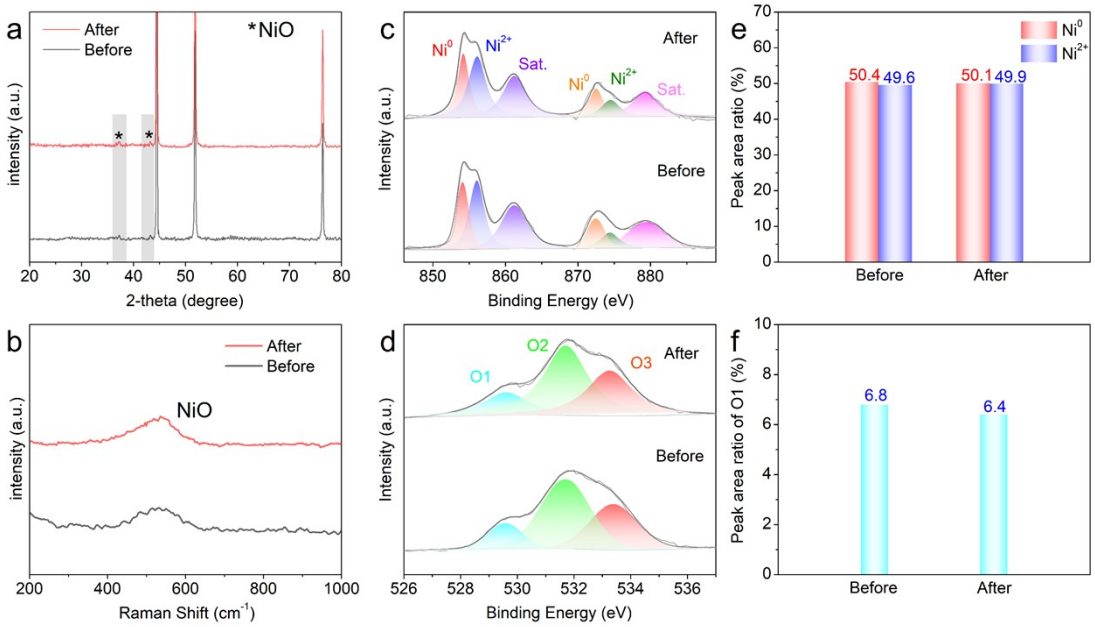

Figure S19. (a) XRD pattern, (b) Raman spectra, (c) XPS spectra of Ni 2p and (d) O 1s after lifetime test, (e) Corresponding proportion of Ni^0 and Ni^{2+}, (f) Corresponding proportion of O1.

We can see that XRD, Raman and XPS of the electrode have not changed significantly after running for a period of time, indicating that the ratio of Ni and NiO has not changed significantly.

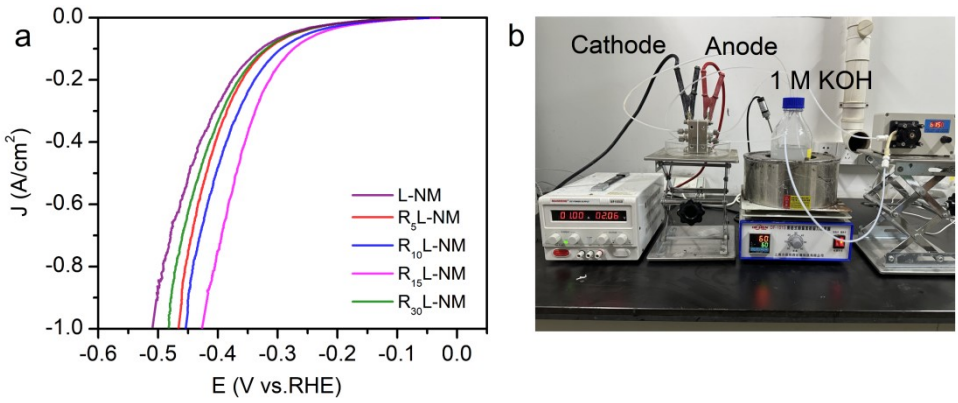

Figure S20. (a) HER activity of L-NM and RL-NM electrodes under AEM conditions (1 M KOH, 60℃). (b) Photograph of the assembled AEM configuration under 1 M KOH, 60℃. (The size of electrode: 1 cm^2).

We also evaluated the activity of electrodes under AEM conditions. The RL-NM electrode displayed the remarkable HER activity in 1 M KOH, 60℃, which is superior to other contrast samples (Fig. S20a). Moreover, the RL-NM and NM were also assembled in AEM configuration. The voltage for RL-NM||NM at 1 A cm^{-2} is 2.06 V (Fig. S20b). Combined results under AWE and AEM conditions, the RL-NM electrode has an appealing potential for industrial application.

Table S1. Peak area ratio of Ni2p with different valence states in L-NM at different reduction time.

Peak area ratio (%)	L-NM	R_5L-NM	R_{10}L-NM	R_{15}L-NM	R_{30}L-NM
Ni^0	30.6	35.1	44.3	50.4	53.5
Ni^{2+}	69.4	64.9	55.7	49.6	46.5

Table. S2 The correlation between composition and performance.

Sample	Ni/NiO ratio	η_{10} (mV)	electrolyte	Faradaic efficiency (%)	Stability
L-NM	0.44	186	1 M KOH	98.8	120 h
R_5L-NM	0.54	169	1 M KOH	99.2	120 h
R_{10}L-NM	0.79	161	1 M KOH	99.0	120 h
R_{15}L-NM	1.01	133	1 M KOH	99.1	120 h
R_{30}L-NM	1.15	176	1 M KOH	99.0	120 h

Table S3. Overpotential comparison of RL-NM with state-of-the-art Ni-based HER catalysts.

Catalyst	η_{10} [mV]	electrolyte	Reference
Ni/NiO NS	226	1 M KOH	[11]
C@NiO/Ni	395	1 M KOH	[12]
NiO_x-AC-500	180	1 M KOH	[13]
Ni/NiO/C	204	1 M NaOH	[14]
Ni NP/Ni-N-C	147	1 M KOH	[15]
NF-Ni_3Se_2/Ni	203	1 M KOH	[16]
Sr-NiO	164	1 M KOH	[17]
Ni/NiO-0.5C	287	1 M KOH	[18]
Ni/NiS	220	1 M KOH	[19]
Ni/NiO-3.8	90	1 M KOH	[9]
NiS_2/MoS_2 HNW	204	1 M KOH	[20]
Ni_2P/Fe_2P	121	1 M KOH	[21]
RL-NM	133	1 M KOH	This work

Table S4. The fitted value of charge transfer resistance for the NiO/L-NM, NM, Raney Ni, L-NM and RL-NM using equivalent circuits.

Sample	R_s (Ω)	R_{ct} (Ω)
NiO/L-NM	0.20	98.76
NM	0.24	75.15
Raney Ni	0.19	8.40
L-NM	0.20	6.83
RL-NM	0.21	3.95

References

1. Kresse, G.; Furthmüller, J. Efficient iterative schemes for ab initio total-energy calculations using a plane-wave basis set. *Phys. Rev. B* 1996, **54**, 11169.

2. Kresse, G.; Furthmüller, J. Efficiency of ab-initio total energy calculations for metals and semiconductors using a plane-wave basis set. *Comput. Mater. Sci*., 1996, **6**, 15.

3. Kresse, G.; Joubert, D. From ultrasoft pseudopotentials to the projector augmented-wave method. *Phys. Rev. B* 1999, **59**, 1758.

4. Perdew, J. P.; Burke, K.; Ernzerhof, M. Generalized Gradient Approximation Made Simple. *Phys. Rev. Lett.* 1996, **77**, 3865.

5. Nørskov, J. K.; Bligaard, T.; Logadottir, A.; Kitchin, J. R.; Chen, J. G.; Pandelov, S.; Stimming, U. Trends in the Exchange Current for Hydrogen Evolution. *J. Electrochem. Soc.*, 2005, **152**, J23.

6. Nørskov, J. K.; Rossmeisl, J.; Logadottir, A.; Lindqvist, L.; Kitchin, J. R.; Bligaard, T.; Jónsson, H. Origin of the Overpotential for Oxygen Reduction at a Fuel-Cell Cathode. *J. Phys. Chem. B*., 2004, **108,** 17886.

7. T. D. Kuhne, M. Iannuzzi, M. Del Ben, V. V. Rybkin, P. Seewald, F. Stein, T. Laino, R. Z. Khaliullin, O. Schutt, F. Schiffmann, D. Golze, J. Wilhelm, S. Chulkov, M. H. Bani-Hashemian, V. Weber, U. Borstnik, M. Taillefumier, A. S. Jakobovits, A. Lazzaro, H. Pabst, T. Muller, R. Schade, M. Guidon, S. Andermatt, N. Holmberg, G. K. Schenter, A. Hehn, A. Bussy, F. Belleflamme, G. Tabacchi, A. Gloss, M. Lass, I. Bethune, C. J. Mundy, C. Plessl, M. Watkins, J. VandeVondele, M. Krack and J. Hutter, *J Chem Phys*, 2020, **152**, 194103.

8. L. Qiao, C. Xi, C. Li, K. Zhang, Q. Li, J. Han and Y. Ding, *Advanced Functional Materials*, 2024, **34**, 2402286,.

9. L. Zhao, Y. Zhang, Z. Zhao, Q.-H. Zhang, L.-B. Huang, L. Gu, G. Lu, J.-S. Hu and L.-J. Wan, *National Science Review*, 2020, **7**, 27-36.

10. W. Zhao, M. Bajdich, S. Carey, A. Vojvodic, J. K. Nørskov and C. T. Campbell, *ACS Catalysis*, 2016, **6**, 7377-7384.

11. A. Y. Faid, A. O. Barnett, F. Seland and S. Sunde, *Electrochimica Acta*, 2020, **361**.

12. A. Chinnappan, J. Dongxiao, W. A. D. M. Jayathilaka, C. Baskar, X. Qin and S. Ramakrishna, *International Journal of Hydrogen Energy*, 2018, **43**, 15217-15224.

13. V. C. Hoang, K. N. Dinh and V. G. Gomes, *Carbon*, 2020, **157**, 515-524.

14. B. Su, Y. Wang, H. Luo, M. Zhong and Z. Lei, *Particle & Particle Systems Characterization*, 2020, **38**.

15. C. Lei, Y. Wang, Y. Hou, P. Liu, J. Yang, T. Zhang, X. Zhuang, M. Chen, B. Yang, L. Lei, C. Yuan, M. Qiu and X. Feng, *Energy & Environmental Science*, 2019, **12**, 149-156.

16. R. Xu, R. Wu, Y. Shi, J. Zhang and B. Zhang, *Nano Energy*, 2016, **24**, 103-110.

17. X. Yi, X. He, F. Yin, G. Li and Z. Li, *Electrochimica Acta*, 2021, **391**.

18. P. Wang, X. Zhang, Y. Wei and P. Yang, *International Journal of Hydrogen Energy*, 2019, **44**, 19792-19804.

19. G. F. Chen, T. Y. Ma, Z. Q. Liu, N. Li, Y. Z. Su, K. Davey and S. Z. Qiao, *Advanced Functional Materials*, 2016, **26**, 3314-3323.

20. P. Kuang, T. Tong, K. Fan and J. Yu, *ACS Catalysis*, 2017, **7**, 6179-6187.

21. Y. Ge, P. Dong, S. R. Craig, P. M. Ajayan, M. Ye and J. Shen, *Advanced Energy Materials*, 2018, **8**.